Supplementary Information: Understanding and Decoupling the Role of Wavelength and Defects in Light-Induced Degradation of Metal-Halide Perovskites

Jeremy Hieulle,[1] Anurag Krishna,[2] Ariadni Boziki,[1] Jean-Nicolas Audinot,[3] Muhammad Uzair Farooq,[1] Joana Ferreira Machado,[1] Marko Mladenović,[4] Himanshu Phirke,[1] Ajay Singh,[1] Tom Wirtz,[3] Alexandre Tkatchenko,[1] Michael Graetzel,[5] Anders Hagfeldt,[2,6] and Alex Redinger[1]

[1]*Department of Physics and Materials Science, University of Luxembourg, Luxembourg City L-1511, Luxembourg*
[2]*Laboratory of Photomolecular Science, Institute of Chemical Sciences and Engineering, École Polytechnique Fédérale de Lausanne, Lausanne 1015, Switzerland*
[3]*Luxembourg Institute of Science and Technology (LIST), Materials Research and Technology (MRT), Advanced Instrumentation for Nano-Analytics (AINA), L-4362 Esch-sur-Alzette, Luxembourg*
[4]*Integrated Systems Laboratory, ETH, Zürich, 8092, Zürich, Switzerland*
[5]*Laboratory of Photonics and Interfaces, École Polytechnique Fédérale de Lausanne, Lausanne 1015, Switzerland*
[6]*Department of Chemistry – Ångström Laboratory, Uppsala University, Box 523, 751 20 Uppsala, Sweden*

Contents

A. Device Performance: $(FAPbI_3)_{0.97}(MAPbBr_3)_{0.03}$ perovskite control sample.

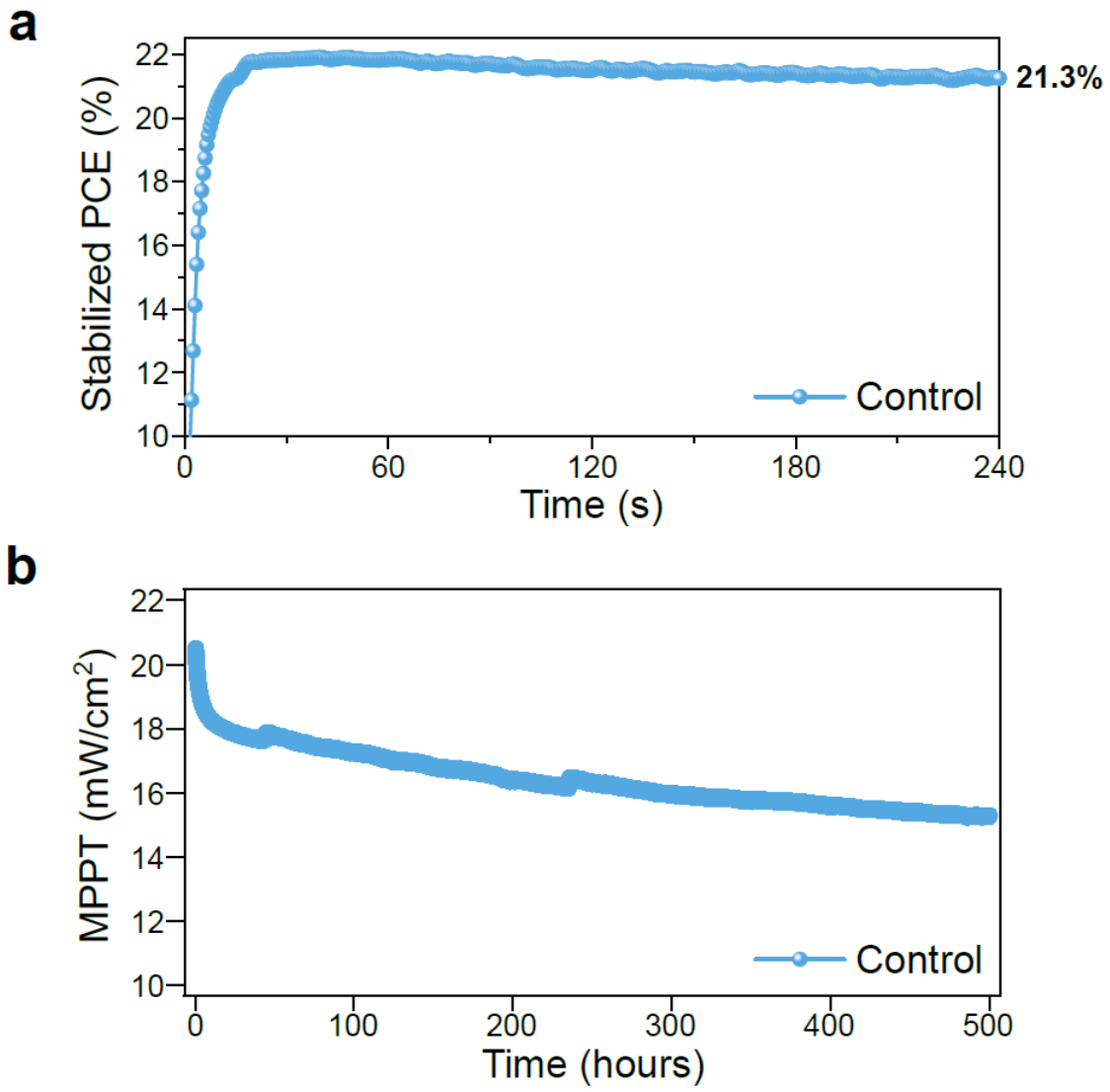

FIG. S1: Device Performance and Stability: (a) Stabilized Power Conversion Efficiency (PCE) for devices made of $(FAPbI_3)_{0.97}(MAPbBr_3)_{0.03}$ non passivated sample (namely, control). (b) Maximum Power Point Tracking (MPPT) over 500 hours under 1 sun illumination. The control perovskite devices retain 75% of the initial power over 500h, showing the long-term stability of the control perovskite sample.

B. 8h Light and then DARK v.s. Continuous Light

We analyzed the degradation of FAPI under continuous white light exposure and compared it with a sampled exposed to an initial 8h Light and then kept in the dark.

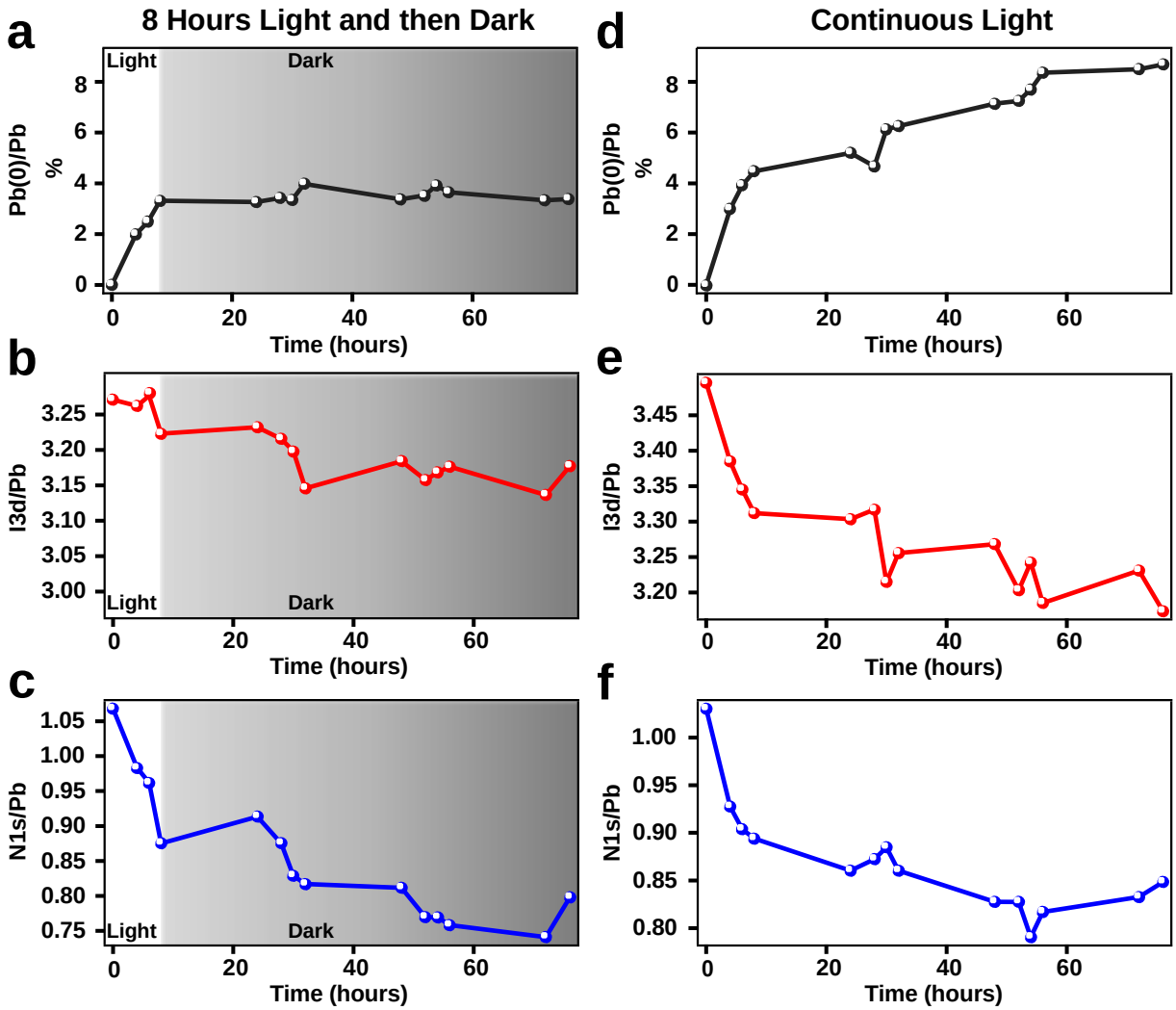

FIG. S2: 8h Light and then DARK v.s. Continuous Light: (a-c) Time evolution of the normalized Pb4f(0), I3d and N1s signal extracted from XPS ratios for a $(FAPbI_3)_{0.97}(MAPbBr_3)_{0.03}$ perovskite sample exposed to white light for an initial time of 8h and then kept in the dark. The ratios were normalized with respect to the total amount of Pb which is assumed to be constant (e.g. $Pb = Pb_{TOT} = Pb(0) + Pb(2+) = constant$). (d-f) Same measurement but for a perovskite sample continuously exposed to white light for a total time of 76 hours. An obvious increase of the Pb(0) signal correlated with a decrease of I3d is observed for the sample continuously exposed to white light.

C. Derivation of the time evolution of $[Pb(2+)]_t$

We consider two consecutive first-order chemical reactions, which are not reversible:

$$FAPI \xrightarrow{k_1} PbI_2 + FAI \tag{1}$$

$$PbI_2 \xrightarrow{k_2} Pb(0) + I_2 \tag{2}$$

Degradation of FAPI is given by:

$$\frac{d[FAPI]_t}{dt} = -k_1[FAPI]_t \tag{3}$$

This equation means that the decompostion of FAPI depends on the concentration of the FAPI present. Solution can be directly written down:

$$[FAPI](t) = [FAPI]_0 \cdot e^{-k_1 t} \tag{4}$$

The amount of PbI_2 depends on how much PbI_2 is generated via decomposition of FAPI (governed by k_1) and how much is transferred to Pb(0) via k_2.

$$\frac{d[PbI_2]_t}{dt} = k_1[FAPI]_t - k_2[PbI_2]_t \tag{5}$$

Equation (4) in (5):

$$\frac{d[PbI_2]_t}{dt} = k_1[FAPI]_0 \cdot e^{-k_1 t} - k_2[PbI_2]_t \tag{6}$$

This is a partial differential equation of the form:

$$\frac{dy(x)}{dx} + k_2 y(x) = k_1 a e^{-k_1 x} \tag{7}$$

Solution:

$$y(x) = \frac{a k_1 e^{-k_1 x}}{k_2 - k_1} + c e^{-k_2 x} \tag{8}$$

This translates into:

$$[PbI_2]_t = \frac{[FAPI]_0 k_1 e^{-k_1 t}}{k_2 - k_1} + c e^{-k_2 t} \tag{9}$$

Find the value of c. Write down solution for t=0.

$$[PbI_2]_0 = \frac{[FAPI]_0 k_1}{k_2 - k_1} + c \tag{10}$$

This gives an expression for $[PbI_2]_t$:

$$[PbI_2]_t = [PbI_2]_0 \cdot e^{-k_2 t} + \frac{[FAPI]_0 \cdot k_1}{k^2 - k^1} e^{-k_1 t} - e^{-k_2 t} \quad (11)$$

We want to plot the variation of Pb(2+) over time. Therefore we need:

$$[Pb(2+)]_t = [PbI_2]_t + [FAPI]_t \quad (12)$$

Use eq.4 and 11:

$$[Pb(2+)]_t = [PbI_2]_0 \cdot e^{-k_2 t} + \frac{[FAPI]_0 \cdot k_1}{k^2 - k^1} e^{-k_1 t} - e^{-k_2 t} + [FAPI]_0 e^{-k_1 t} \quad (13)$$

From the above equation, it is possible to estimate the evolution of the Pb(0) concentration overtime $[Pb(0)]_t$, such as:

$$[Pb(2+)]_t + [Pb(0)]_t = Pb_{TOT} = 100\% \quad (14)$$

From the amount of Pb(0) generated it is then possible to estimate the change in I and FA content following the two step chemical reaction depicted earlier. For each Pb(0) generated there should be 1 FAI molecule that is dissociated from the perovskite, while I_2 is released (equations 1 and 2). This means that each time a Pb(0) is generated we should observe a decrease of 2 nitrogens and 3 iodines in the XPS signal.

The comparison between the I and FA content recorded experimentally by XPS and their expected amount from our model is depicted in table I.

	RT light	LT light	dark	calc RT	calc LT
I (g)	13 ↓	7 ↓	1 ↓	45 ↓	12 ↓
Pb(0) (s)	11.5 ↑	5.4 ↑	1 ↑	15 ↑	4 ↑
FA (g)	16.5 ↓	15.5 ↓	4 ↓	15 ↓	4 ↓

TABLE I: Cross-check the consistency of the model by comparing the I and FAI content measured in the experiment and the expected I and FA amount estimated from our two-step reaction model. The calculated values were estimated by assuming no initial PbI_2. All the values in the table are percentages (%).

D. Degradation of PbI_2 followed by XPS

We analyzed by XPS the degradation of a PbI_2 film on Au/mica under white light exposure.

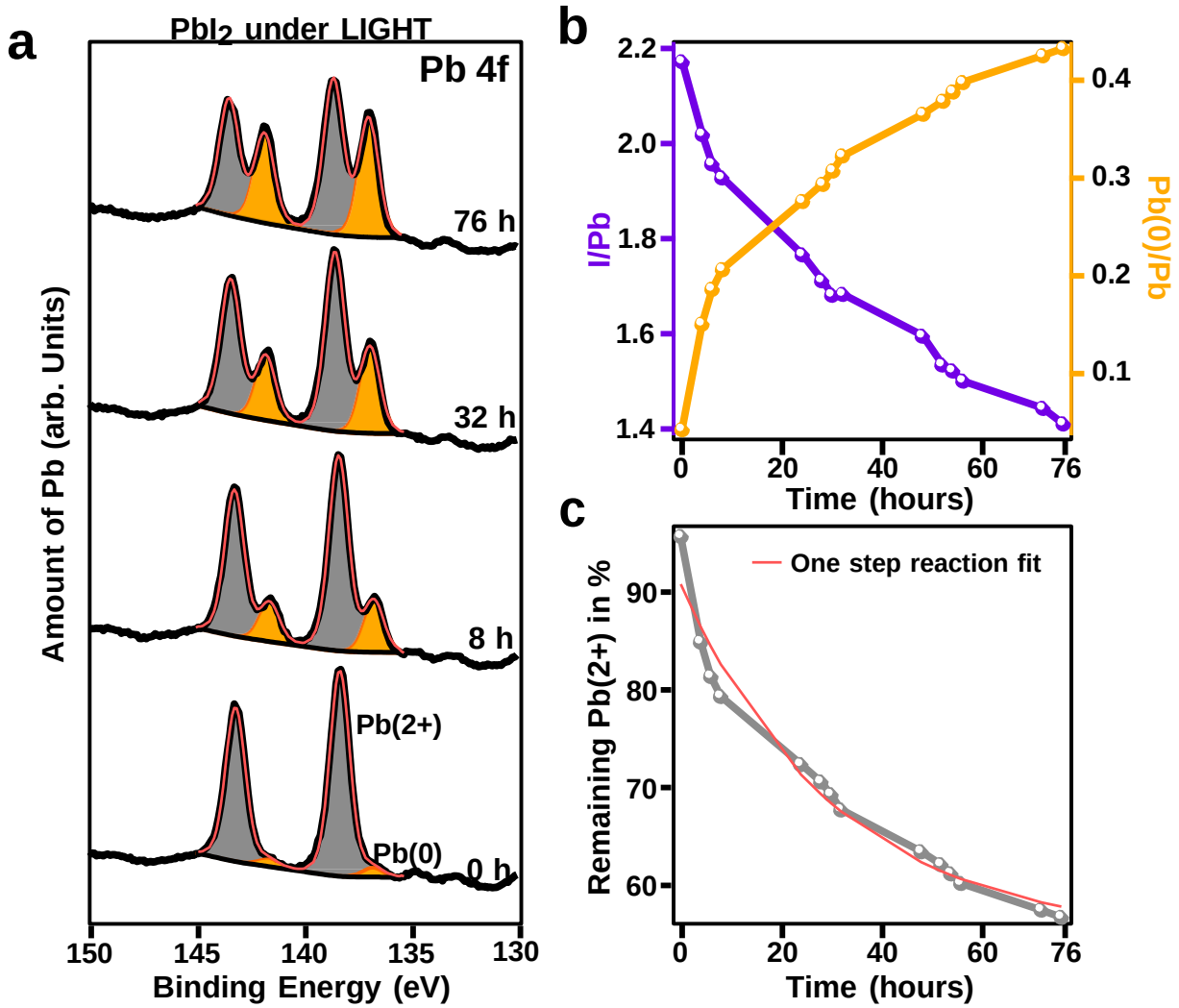

FIG. S3: Evolution of Pb(0) signal in a PbI_2/Au(111)/mica film exposed to continuous white light, v.s. time. (a) Selected XPS spectra taken at distinct time intervals for the Pb4f core level. For better readability, the XPS spectra obtained at distinct times were vertically shifted, while the Pb(0) oxidation states were highlighted in orange. (b) The normalized I3d and Pb(0) signal extracted from XPS as a function of time. The ratios were normalized with respect to the total amount of Pb which is assumed to be constant (e.g. $Pb = Pb_{TOT} = Pb(0) + Pb(2+) = constant$). A clear correlation exists between the generation of Pb(0) and the loss of I3d signal. (c) Time evolution of the remaining Pb(2+). The solid red curve denote a exponential decay fit: $[PbI_2](t) = [PbI_2]_{init} \times (exp(-k_0 \times t))$, considering a first order and one step chemical reaction: $PbI_2 \rightarrow Pb(0) + I_2$.

E. Large Scale AFM/KPFM in N2 environment

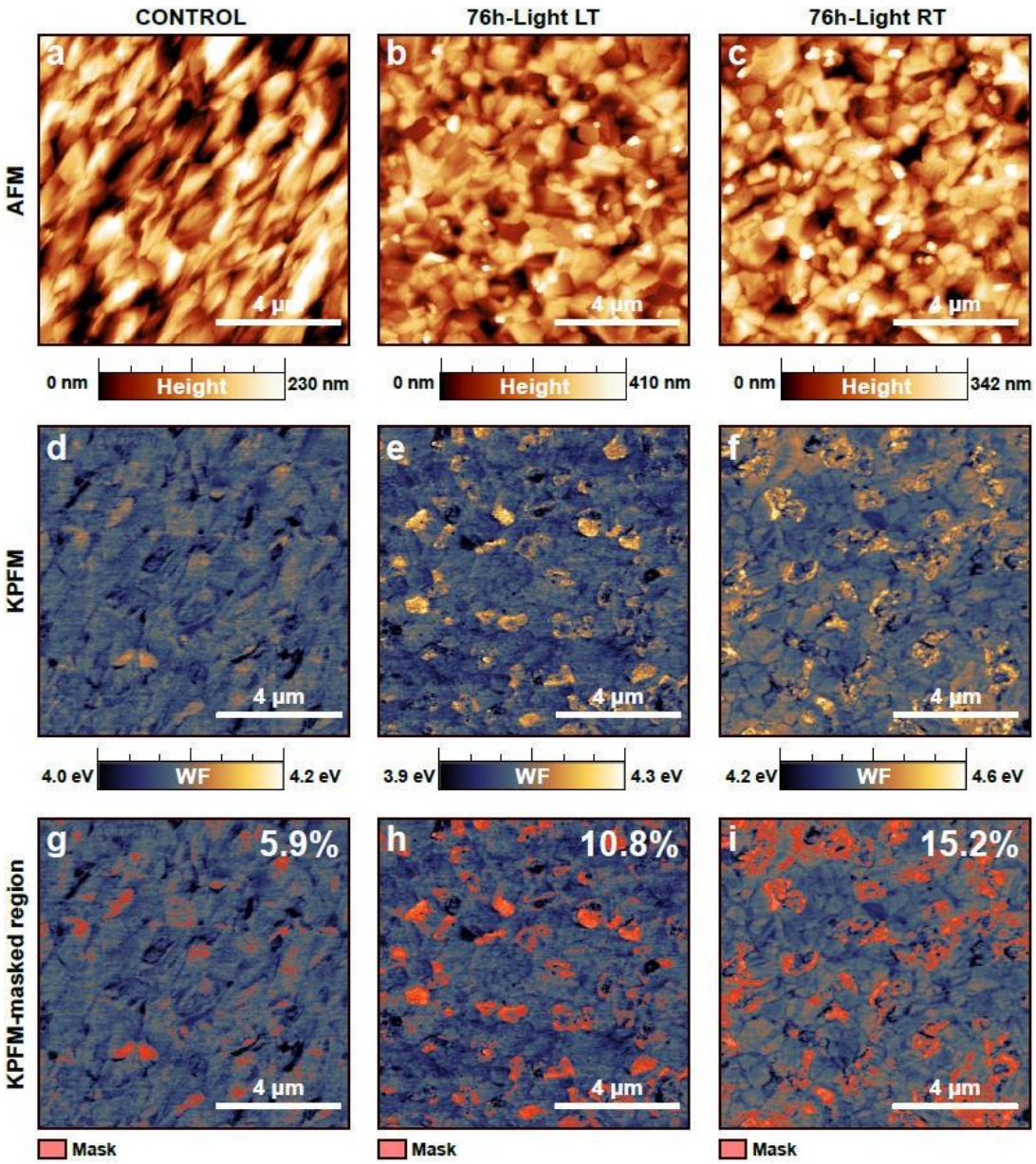

FIG. S4: Correlation between granular domains and higher workfunction. (a-c) Wide range topographic images recorded by AFM for $(FAPbI_3)_{0.97}(MAPbBr_3)_{0.03}$ samples kept respectively in the dark (labelled as: control), under white light for 76h at a temperature of $-70^{\circ}C$ (labelled as: 76h-Light LT), and under white light for 76h at room temperature of (labelled as: 76h-Light RT). (d-f) Corresponding workfunction maps obtained by KPFM on the same areas. Higher workfunction correlate with the presence of granular domains in the topographic image. (g-i) Overlay red mask used to determine the percentage of high workfunction domains covering the surface of each sample. A higher proportion of high workfunction domains (e.g. granular structure) are observed for the light-degraded samples (respectively 10.8% and 15.2% for LT and RT samples), as compared to control (5.9%).

F. Comparison of pristine and degraded FAPI by High-Resolution EM imaging

High-resolution EM images show a clear contrast between the pristine and degraded $(FAPbI_3)_{0.97}(MAPbBr_3)_{0.03}$ samples (abbreviated as FAPI). The appearance of granular structures are clearly visible after 76h of exposure to white light.

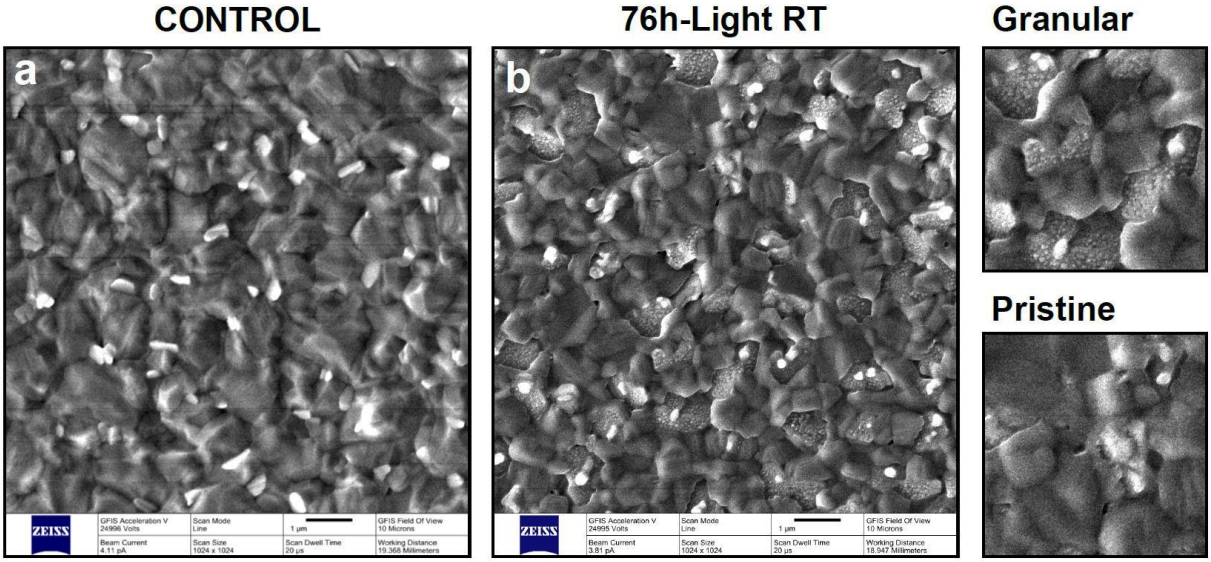

FIG. S5: High-resolution EM images. (a) non-degraded $(FAPbI_3)_{0.97}(MAPbBr_3)_{0.03}$ sample kept in the dark (namely, control). (b) Perovskite film degraded under white light for 76 hours at room temperature (namely, 76h-Light RT). High brightness domains appear in the Control sample associated to high workfunction PbI_2 rich domains. After degradation, granular domains grow around the PbI_2 rich regions, acting like nucleation points. Pristine and granular domains obtained for the light-degraded sample are compared in the right insets of Figure b.

G. Raw SIMS images without marked areas

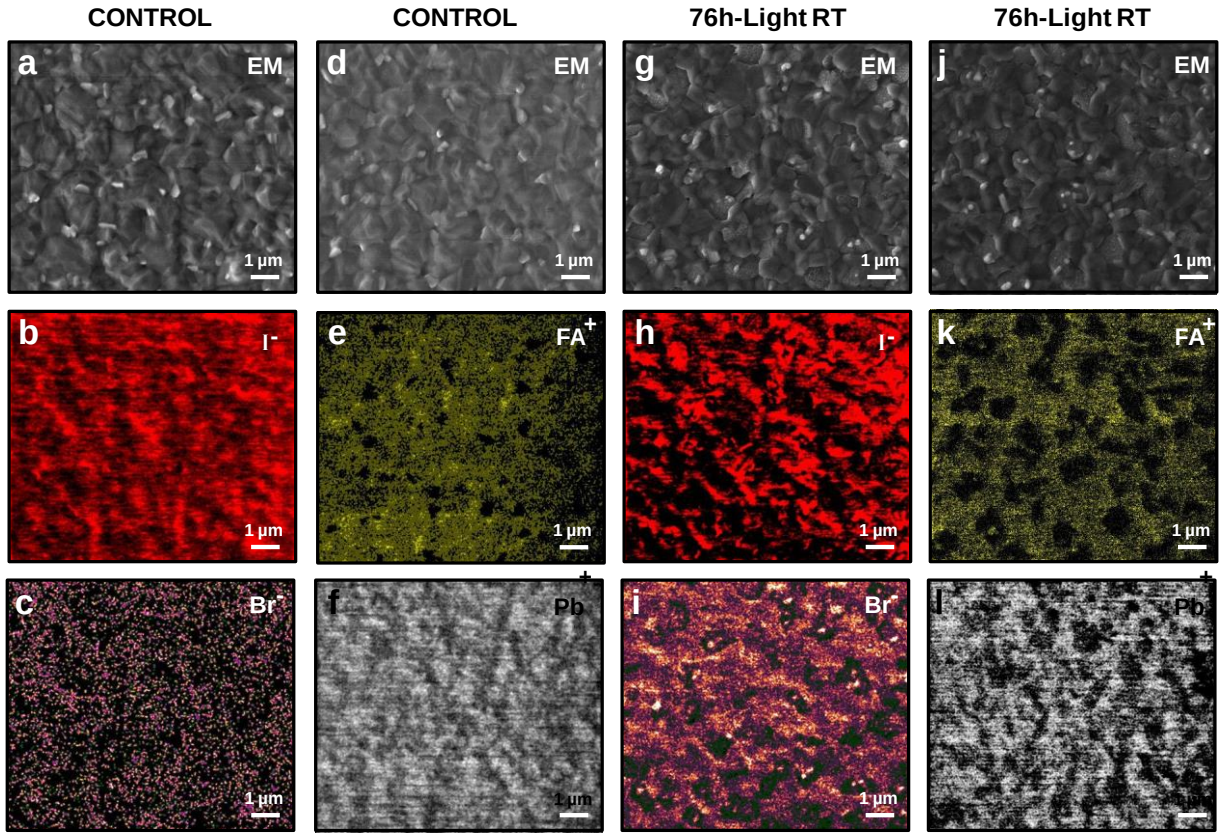

FIG. S6: Variation of composition before/after light-induced degradation without marked regions. (a-c) EM image of a non-degraded $(FAPbI_3)_{0.97}(MAPbBr_3)_{0.03}$ sample kept in the dark (namely, control) and the corresponding SIMS maps for iodine (I) and bromine (Br) obtained for negative polarity. (d-f) EM image and SIMS maps (FA and Pb) of the same control sample on a different macroscopic location after switching the beam to positive polarity. (g-i) EM image of a perovskite sample degraded under white light for 76 hours at room temperature (namely, 76h-Light RT) and the corresponding SIMS maps for iodine (I) and bromine (Br). (j-l) EM image and SIMS maps (FA and Pb) of the same 76h-Light RT degraded sample on a different macroscopic location. Those SIMS measurements are identical to the ones depicted in the main manuscript but without overlay or marked regions (e.g. row data).

H. Oxygen and C-N signal in SIMS for Pristine and Degraded FAPI

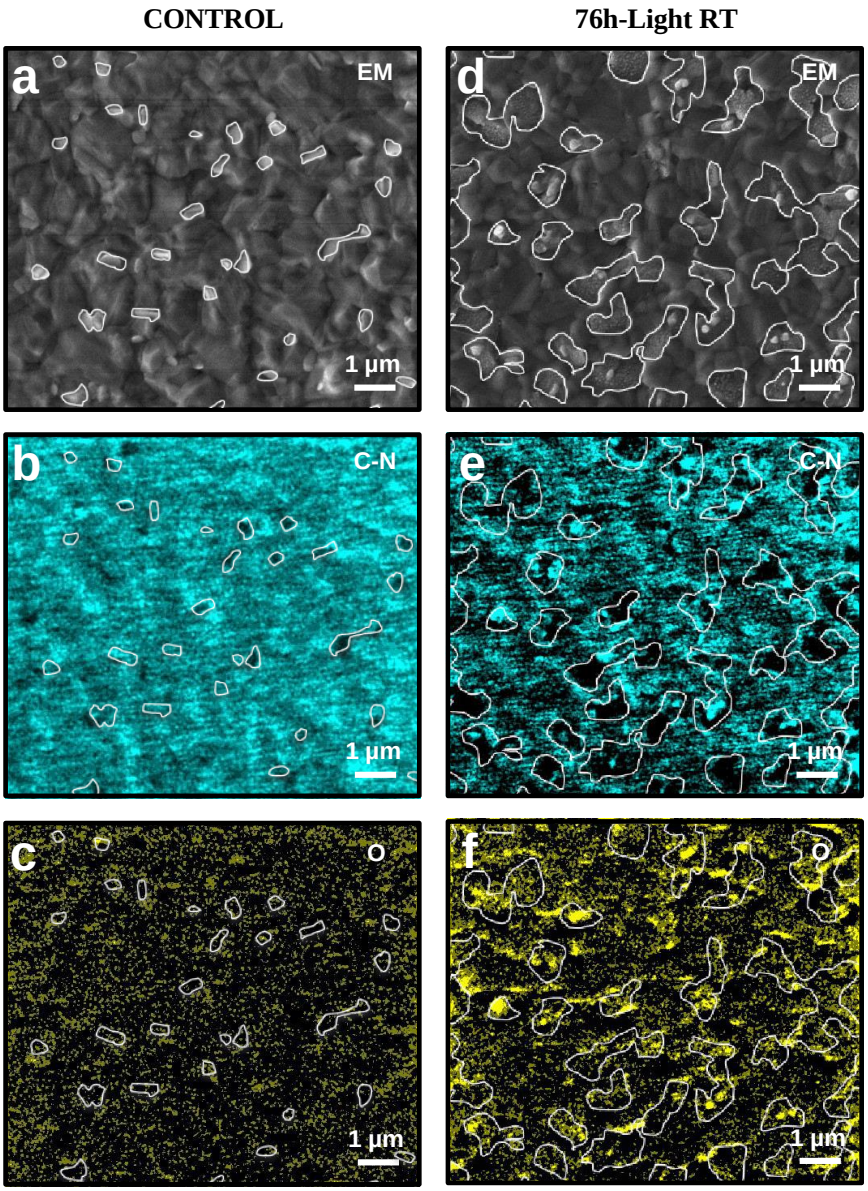

FIG. S7: Oxygen and Carbon-Nitrogen composition before/after light-induced degradation (a-c) EM image of a non-degraded $(FAPbI_3)_{0.97}(MAPbBr_3)_{0.03}$ sample kept in the dark (namely, control) and the corresponding SIMS maps for organic compounds (C-N) and oxygen (O). (d-f) EM image of a perovskite sample degraded under white light for 76 hours at room temperature (namely, 76h-Light RT) and the corresponding SIMS maps for organic compounds (C-N) and oxygen (O).

I. Energy Calculation for Vk center defect formation in bulk PbI_2 under light exposure

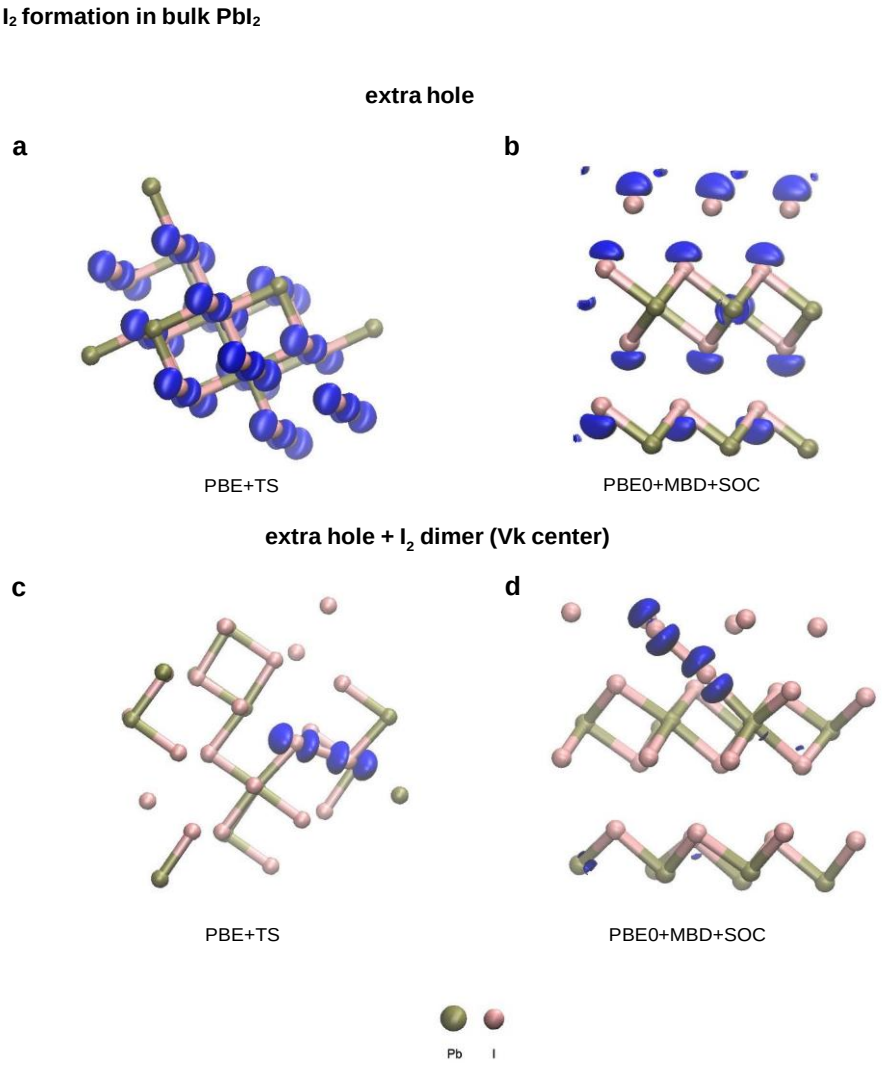

FIG. S8: Charge densities representing the Valence Band Maximum (VBM) of bulk PbI_2. (a,b) Charge densities in the presence of an extra hole while no defect has been introduced in the structure (a - protocol of PBE+TS, b – protocol of PBE0+MBD+SOC). The charge densities are delocalized. (c,d) Charge densities in the presence of an extra hole and of a Vk center defect formed by moving closer two iodine ions. The distance between the two iodine ions is kept constant during the calculation at 3.2Å(c - protocol of PBE+TS, d – protocol of PBE0+MBD+SOC). The charge densities are localized on the defect.

To determine the impact of light and defects on the degradation of PbI_2 domains, two types of calculations have been performed. First, to simulate the impact of light we introduced an extra hole in defect-less PbI_2 domains and relaxed the structure. In that case, we found that the extra hole is delocalized all over the structure, preventing degradation through hole-trapping (Figure S8 a).

Second, we studied the formation of I_2^- dimer as a potential mechanism for the degradation of PbI_2. Aiming at forming a Vk center defect, we moved closer two iodine ions until the distance between them is 3.2 Å. In that case, we found that when an extra hole is introduced (e.g., light shining on), it localizes on the Vk center defect (Figures S8 c), allowing PbI_2 degradation through hole-trapping.

We then calculated the defect formation energy utilizing the PBE functional augmented with long-range van der Waals (vdW) corrections based on the Tkatchenko-Scheffler [1] method (PBE+TS). A positive formation energy of 0.47 eV was found, thus indicating that the dimer will not form spontaneously. To this end, spontaneous hole-trapping through the formation of I_2^- dimer has not been observed. However, if the Vk center defect has already been created (through other external factors), the hole can localize on it.

In other words, the presence of Vk center defects will facilitate the degradation of PbI_2 domains under light-exposure by promoting hole-trapping.

Similar findings were obtained for more accurate calculations protocols Using PBE0+MBD+SOC (Figures S8 b,d) with/without Vk center defects.

J. STS and dI/dV maps on the LT degraded FAPI sample

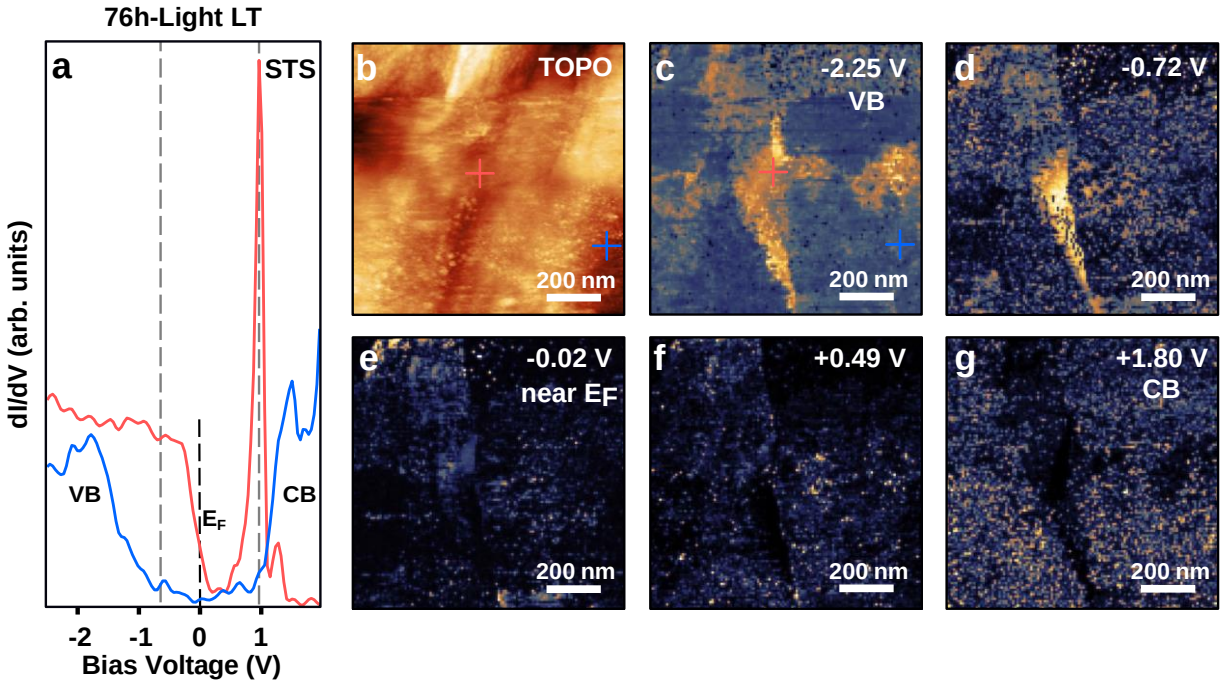

FIG. S9: Bandgap variation at the nanoscale on the 76h-Light LT degraded $(FAPbI_3)_{0.97}(MAPbBr_3)_{0.03}$ perovskite film (a) Scanning tunneling spectroscopy (STS) recorded on the position marked with blue/red crosses in the topographic image and dI/dV map, in b and c respectively. Similar bandgap reduction was observed on the 76h-Light RT degraded perovskite sample, as depicted in the main manuscript. (b-g) Topographic STM image and corresponding dI/dV (conductance) maps recorded at various sample voltages (energies). Typical lock-in parameters are as follows: $V_{mod} = 20mV$; $Frequency = 965Hz$; $sensitivity = 500mV$; and $time\ constant = 10ms$. Tunneling parameters are $I_t = 0.1nA$; $Bias = -1.5V$.

K. Evolution of Iodine, FA and Pb(0) content for passivated films without and with wavelength selective filters

	Pa passivated	Pa + band pass [304-785]nm	Pa + long pass 590nm	Pa + dark
I (g)	11.5 ↓	4.5 ↓	3.2 ↓	5 ↓
Pb(0) (s)	5.5 ↑	2.5 ↑	2 ↑	1.8 ↑
FA (g)	26 ↓	23 ↓	19 ↓	22 ↓

TABLE II: Evolution of the I, FAI and Pb(0) content for the passivated sample with an organic biphenyl-4,4'-dithiol layer (labelled Pa). A comparison of the samples with and without wavelength selective filters is given. Two types of filters were used: a band pass filter ($304 \leq \lambda \leq 785$ nm), and a long pass filter ($\lambda \geq 590$ nm). All the values in the table are percentages (%).

L. Methods

1. Precursor Materials and substrates used

Fluorine-doped tin oxide (FTO, 4.0 mm-thick, 10 Ω/sq) conductive glass was purchased from Nippon Sheet Glass (NSG). Lead iodide (PbI_2) was purchased from Alfa Aesar. Formamidinium iodide (FAI) and titanium dioxide paste (TiO_2-30 NRD) were purchased from Greatcell. 2,2',7,7'-Tetrakis[N,N-di(4-methoxyphenyl)amino]-9,9'-spirobifluorene (Spiro-OMeTAD, > 99.5 %) was purchased from Xi'an Polymer Light Technology Corp. Methylammonium lead tribromide ($MAPbBr_3$) was purchased from Share Chem. 4-tert-butyl pyridine (tBP, 96 %), lithium bistrifluorosulfonylimide (LiTFSI, 99.95 %), acetonitrile (ACN), titanium diisopropoxide bis(acetylacetonate) 75 wt. % in isopropanol, acetylacetone, and methylammonium chloride (MACl) were purchased from Sigma-Aldrich. Ultra-dry dimethylformamide (DMF), dimethyl sulfoxide (DMSO), ethanol (EtOH), diethyl ether, and chlorobenzene (CB) were purchased from Acros. All the chemicals were used as received without further purification.

2. Perovskite Precursor Solution Preparation

$(FAPbI_3)_{0.97}(MAPbBr_3)_{0.03}$ precursor solution was prepared by dissolving PbI_2 (735 mg), FAI (252 mg), $MAPbBr_3$ (21.6 mg), and MACl (33.8 mg) in 1 mL of DMF-DMSO mixed solution (DMF:DMSO volume ratio 8:1). The solution was heated at 70 °C for ≃ 4 hours.

3. Device Fabrication

Zinc powder and 4 M hydrorchloric acid were used to pattern FTO glass substrates. The substrates were then cleaned in an ultrasonic bath using 2% Hellmanex detergent solution, deionized water, acetone, and ethanol for 15 min each, and dried with an air blowgun. A 20-40 nm thick TiO_2 (c-TiO_2) layer was applied by spray pyrolysis to 30 min O_3/UV treated substrates. The precursor solution, prepared by diluting 75 wt.% diisopropoxide bis(acetylacetonate) with ethanol in a volume ratio 1:9 and adding 4 vol. % acetylacetone, was applied to the substrates using oxygen as a carrier gas. 100 to 150 nm thick mesoporous TiO_2 (mp-TiO_2) layer was obtained by spin-coating ethanol suspension (1:6, weight ratio) of a commercial paste (Dyesol 30 NR-D) at 5000 rpm for 15 s. The films were dried at 80 °C for 10 min, gradually heated, and then sintered at 450 °C for 30 min. After cooling down to room temperature, 100 μl of 0.1 M solution of Li-TFSI in acetonitrile was spin-coated at 3000 rpm for 20 s, sintered at 450 °C for 30 min, and cooled down to 150 °C. Perovskite films were deposited to mp-TiO_2 in a dry-air glovebox (RH < 15 %) by spin-coating 50 μl of the precursor solution in a two-step process at 1000 rpm for 10 s and 5000 rpm for 25 s. 500-600 μl of diethylether was dropped on the spinning substrate 10 s before the end of the second step. The substrates were then heated at 150 °C for 20 min. Molecular passivation solutions were prepared by dissolving 3 mg in 1 ml of chlorobenzene, then heated for 2 h at

70 °C and cooled down to room temperature. Perovskite surface was treated with the ligand by dynamically spin-coating (dynamic spin-coating implies that the solution was added to a spinning substrate) 80 μl of the solution at 4000 rpm for 25 s, after which the substrate was heated at 100 °C for 3 min. 50 μl of 75 mM spiro-OMeTAD solution in chlorobenzene with 40 mM Li-TFSI, and 270 mM tBP as additives was dynamically spin-coated at 4000 rpm for 25 s to form the HTL. Thermal evaporation was used to obtain an approximately 80 nm thick gold electrode.

4. *Photovoltaic performance measurements of the device*

A 300 W Xenon light source (Oriel) was calibrated using Schott K113 Tempax filter (Prazosopms G; as & Optik GmbH) for the spectral mismatch between the solar simulator, and the AM 1.5G spectrum. The light intensity was calibrated using a silicon photodiode before each measurement. Keithley 2400 source measure unit was used for measuring current voltage scan. The unit applied an external voltage bias and measured the response current at a rate of 50 mV/s. The area of the devices was 0.25 cm^2 (0.5 cm $\times$ 0.5 cm), and the cells were masked with a black metal mask (0.158 cm^2). The cells were not preconditioned before the measurements (e.g., light soaking or voltage bias). A commercial apparatus (Arkeo-Ariadne, Cicci Research s.r.l.) based on a 300W Xenon lamp was used for recording external quantum efficiency (EQE) spectra. The glass side of champion devices was coated with an antireflection film.

5. *Stability measurements on the full device stack*

The stability data was acquired from maximum power point (MPP) tracking of the un-encapsulated devices under a continuous nitrogen flow at room temperature. This was done under a white light-emitting diode lamp with biologic MPG2 potentiostat. The device area was masked to around 0.09 cm^2. The light intensity was around 100 mW/cm^2.

6. *X-ray Photoelectron Spectroscopy: XPS*

XPS measurements were performed in ultra-high vacuum (UHV) conditions, at a base pressure of 5.0×10^{-10}mbar. A magnesium K_a source with a photon energy of 1253.6 eV was used. All the measurements were performed with strictly the same X-ray exposure time (1h) and power (300 Watts) to prevent the influence of beam damages. The XPS spectra were recorded with a Prevac (Upper Silesia, Poland) analyzer, using a single channeltron. Casa XPS software was used to fit and analysed the data. The Pb4f core level was used to track the chemical decomposition of the perovskite film under light exposure through the appearance of low degree of oxidation peaks (namely Pb(0)).

7. Atomic and Kelvin Force probe microscopy: AFM & KPFM

The AFM and KPFM maps presented in Figure 2 (main manuscript) were obtained in UHV in frequency modulation mode with a fixed excitation amplitude of 0.5V. The cantilever used has a Q factor of 38000 in UHV. For KPFM measurements an external lock-in amplifier was employed to measure the contact potential difference (CPD) between the tip and the sample. The typical lock-in parameters used are as follows: a modulation voltage of 0.4 V, a time constant of 1 ms, an excitation frequency of 965 Hz, and sensitivity of 5 ms.

The KPFM and AFM measurements were repeated under nitrogen environment to study topography and workfunction variations on a larger length scale (Figure S4), as compared to the UHV measurement. The relative humidity during the measurements was less than 10%, without exposing the samples to air. By combining KPFM with non-contact AFM, the topography and CPD measurements were acquired simultaneously over the same area of the sample. AFM measurements were conducted in the amplitude-modulation mode, while the KPFM signal was obtained in frequency modulation.

8. Electron Microscopy and Secondary Ion Mass Spectrometry: EM & SIMS

The EM and SIMS measurements were acquired by using a Helium Ion Microscope (HIM) (Nanofab, Zeiss, Peabody, Ma, US), coupled with a Secondary Ion Mass Spectrometer developed at LIST [2]. The gas Field Ion Source (GFIS) of the HIM allows producing finely focused Helium and Neon primary beams. A short exposure to ambient conditions prior to the measurements was unavoidable in order to load the samples in the microscope chamber. Secondary electron (SE) images were acquired with a Helium beam (25keV He^+, 3.8pA) and SIMS images with a Neon Beam (20keV, 7pA). SE images were acquired before SIMS acquisition on the same microscopic areas. For the detection of positive ions (FA fragment at the mass m/z = 43 and Lead at the m/z = 208), and negative ions (Oxygen at the m/z = 16, Bromine at the mass m/z = 79 and Iodine at the mass m/z = 127), the sample was biased positively and negatively, respectively.

9. Scanning Tunneling Microscopy and Spectroscopy: STM & STS

STM and STS measurements were performed in the same UHV setup as the AFM/KPFM and XPS, preventing any oxygen ingress or any undesirable contamination. A chemically-etched tungsten tip was used to acquire both the topographic images and conductance maps/spectra. A lock-in amplifier was used to provide a direct measurement of the derivative of the I/V characteristic. This approach allows for a better signal-to-noise ratio, and provides information about the local density of states [3, 4] of the sample. Typical lock-in parameters during the STS measurements are: sensitivity= $500mV$, voltage modulation= $20mV$, time constant= $10ms$, Frequency= $965Hz$, current set-point= $0.1nA$, starting voltage= $-1.5V$, acquisition time= $1s$ per spectrum/pixel. All STM/STS measurements were performed at room temperature. The data analysis has been performed using WSxM [5] and Gwyddion [6] software.

10. Computational Details

For the pure perovskite phase of $FAPbI_3$ previous 0 K static DFT calculations revealed that among α and β $FAPbI_3$ phases, β-$FAPbI_3$ has lower energy, for this reason, the β phase was considered in our analysis [7]. Regarding PbI_2 and FAI crystal structures, those have been retrieved from the database of the Cambridge Crystallographic Data Center (CCDC). The DFT calculations have been performed using the Quantum Espresso suites of codes [8, 9]. For the dissociation enthalpy calculation, GGA to DFT in the PBE formulation has been used [10]. In this case, SOC effects were not explicitly included in the calculations because of the well-known fortuitous error cancellation of SOC and many-body effects in the case of 3D lead halide perovskites when PBE functional is used [11]. The interactions between valence electrons and core electrons and nuclei were described by ultrasoft pseudopotentials [12]. The Kohn-Sham orbitals are expanded in a plane wave basis set with a kinetic energy cutoff of 40 Ry and a density cutoff of 240 Ry. For $FAPbI_3$, PbI_2, and FAI the Brillouin zone was sampled with a 1x1x2, 2x2x2, and 1x1x2 Monkhorst-Pack k-points shifted grid, respectively [13]. These values have been chosen after having performed convergence tests for the total energy, the band gap, the pressure, the stresses, and the atomic forces. Regarding the calculations about the localization and delocalization of a hole, the same computational scheme was used for $FAPbI_3$. However, in the case of PbI_2 a different protocol was applied. The fortuitous error cancellation of SOC and many-body effects do not apply to a system such as PbI_2 which is 2D. Hence DFT in the PBE formulation together with the TS scheme for the treatment of vdW has been applied [1]. The interactions between valence electrons and core electrons and nuclei were described by norm-conserving pseudopotentials [12]. The Kohn-Sham orbitals were expanded in a plane wave basis set with a kinetic energy cutoff of 80 Ry and a density cutoff of 320 Ry. For $FAPbI_3$ and PbI_2 the Brillouin zone was sampled with a 2x2x4, and 4x4x2 Monkhorst-Pack k-points shifted grid, respectively [13]. The defect formation energy was calculated as the difference between the energies of the defect-containing structure and the pristine structure both having a +1 charge, (representing the extra hole). In the case that the PBE0+MBD+SOC protocol was employed; the all-electron numeric-atom-centered orbital code FHI-aims (Fritz Haber Institute ab initio molecular simulations) was used [14]. Scalar relativistic effects were included by means of the zero-order regular approximation (ZORA). For all calculations we used the tight species default settings in FHI-aims, for all numerical atom-centered basis functions and integration grids. For $FAPbI_3$, PbI_2, and FAI the Brillouin zone was sampled with a 3x3x3, 2x2x2, and 4x3x4 Monkhorst-Pack k-points grid, respectively. Convergence criteria of 10^{-6} eV, 10^{-6} electrons/Å^3, 10^{-4} eV/Å, and 10^{-3} eV were used for the total energy, charge density, forces, and sum of eigenvalues, respectively. These values have also been chosen after having performed convergence tests for the total energy, the pressure, the stresses, and the atomic forces.

REFERENCES:

[1] A. Tkatchenko and M. Scheffler, Phys. Rev. Lett. 102, 073005 (2009).

[2] J.-N. Audinot, P. Philipp, O. D. Castro, A. Biesemeier, Q. H. Hoang, and T. Wirtz, Reports on Progress in Physics 84, 105901 (2021).

[3] J. Bardeen, Phys. Rev. Lett. 6, 57 (1961).

[4] J. Tersoff and D. R. Hamann, Phys. Rev. Lett. 50, 1998 (1983).

[5] I. Horcas, R. Fernández, J. M. Gómez-Rodríguez, J. Colchero, J. Gómez-Herrero, and A. M. Baro, Review of Scientific Instruments 78 (2007), 10.1063/1.2432410.

[6] D. Nečas and P. Klapetek, Central European Journal of Physics 10, 181 (2012).

[7] A. Boziki, M. Mladenović, M. Grätzel, and U. Rothlisberger, Phys. Chem. Chem. Phys. 22, 20880 (2020).

[8] P. Giannozzi, S. Baroni, N. Bonini, M. Calandra, R. Car, C. Cavazzoni, D. Ceresoli, G. L. Chiarotti, M. Cococcioni, I. Dabo, A. D. Corso, S. de Gironcoli, S. Fabris, G. Fratesi, R. Gebauer, U. Gerstmann, C. Gougoussis, A. Kokalj, M. Lazzeri, L. Martin-Samos, N. Marzari, F. Mauri, R. Mazzarello, S. Paolini, A. Pasquarello, L. Paulatto, C. Sbraccia, S. Scandolo, G. Sclauzero, A. P. Seitsonen, A. Smogunov, P. Umari, and R. M. Wentzcovitch, Journal of Physics: Condensed Matter 21, 395502 (2009).

[9] P. Giannozzi, O. Andreussi, T. Brumme, O. Bunau, M. B. Nardelli, M. Calandra, R. Car, C. Cavazzoni, D. Ceresoli, M. Cococcioni, N. Colonna, I. Carnimeo, A. D. Corso, S. de Gironcoli, P. Delugas, R. A. DiStasio, A. Ferretti, A. Floris, G. Fratesi, G. Fugallo, R. Gebauer, U. Gerstmann, F. Giustino, T. Gorni, J. Jia, M. Kawamura, H.-Y. Ko, A. Kokalj, E. Küçükbenli, M. Lazzeri, M. Marsili, N. Marzari, F. Mauri, N. L. Nguyen, H.-V. Nguyen, A. O. de-la Roza, L. Paulatto, S. Poncé, D. Rocca, R. Sabatini, B. Santra, M. Schlipf, A. P. Seitsonen, A. Smogunov, I. Timrov, T. Thonhauser, P. Umari, N. Vast, X. Wu, and S. Baroni, Journal of Physics: Condensed Matter 29, 465901 (2017).

[10] J. P. Perdew, K. Burke, and Y. Wang, Phys. Rev. B 54, 16533 (1996).

[11] J. Even, L. Pedesseau, J.-M. Jancu, and C. Katan, The Journal of Physical Chemistry Letters 4, 2999 (2013), https://doi.org/10.1021/jz401532q .

[12] A. Dal Corso, Computational Materials Science 95, 337 (2014).

[13] H. J. Monkhorst and J. D. Pack, Phys. Rev. B 13, 5188 (1976).

[14] V. Blum, R. Gehrke, F. Hanke, P. Havu, V. Havu, X. Ren, K. Reuter, and M. Scheffler, Computer Physics Communications 180, 2175 (2009).